Advanced Journal of Chemistry, Section A

Journal homepage: www.ajchem-a.com

Original Research Article

Structure-Based Design and Characterization of Cyclosenegalin Derivatives as Novel Breast Cancer Therapeutics

Jajang Japar Sodik[1,*], Kania Fajarwati[2], Farendina Suarantika[3], Taufik Muhammad Fakih[4], Rani Maharani[5], Dhania Novitasari[6]

[1]*Department of Pharmaceutical Analysis and Medicinal Chemistry, Faculty of Pharmacy, Universitas Bhakti Kencana, Jalan Soekarno-Hatta No.754, Bandung, 40614, Indonesia*
[2]*Department of Pharmaceutical Biology, Faculty of Pharmacy, Universitas Bhakti Kencana, Jalan Soekarno-Hatta No.754, Bandung, 40614, Indonesia*
[3]*Pharmacist Professional Education Study Program (PPSP), Faculty of Mathematics and Natural Sciences, Universitas Islam Bandung, Jalan Batik Halus, Bandung, 40123, Indonesia*
[4]*Department of Pharmacy, Faculty of Mathematics and Natural Sciences, Universitas Islam Bandung, Jalan Ranggagading, Bandung, 40116, Indonesia*
[5]*Department of Pharmaceutical Analysis and Medicinal Chemistry, Faculty of Pharmacy, Universitas Padjadjaran, Jalan Raya Bandung Sumedang KM 21, Sumedang, 45363, Indonesia*
[6]*Department of Chemistry, Faculty of Mathematics and Natural Sciences, Universitas Padjadjaran, Jalan Raya Bandung Sumedang KM 21, Sumedang, 45363, Indonesia*

ARTICLEINFO

Article history

Submitted: 2025-11-16
Revised: 2025-12-06
Accepted: 2026-01-05
ID: AJCA-2511-1971
DOI: **10.48309/AJCA.2026.560035.1971**

KEYWORDS

Cyclosenegalin A
Solid-phase peptide synthesis
Molecular docking
MTT assay
Antiproliferative activity

ABSTRACT

Triple-negative breast cancer (TNBC), which lacks ER, PR, and HER2 expression, remains challenging to treat due to the absence of targeted therapeutic options and frequent chemoresistance. Cyclosenegalin A, a cyclic heptapeptide, offers a compact *β*-turn scaffold amenable to selective receptor engagement but displays only moderate native activity. In this study, computational modeling, chemical synthesis, and cell-based evaluation were integrated to develop cyclosenegalin-derived peptides as anticancer candidates. A 29-member analog panel was sketched in ChemDraw, converted to 3D in Chem3D, and subjected to geometry and frequency optimization using Gaussian (DFT B3LYP/3-21G) to afford electronically stable conformers. Molecular docking with AutoDock Vina against ERα (PDB: 3ERT), PR (2OVH), EGFR kinase (2ITY), and the IκBα/NF-κB complex (1NFI) identified two multi-target leads, A14 and A21, which exhibited consistently lower predicted binding free energies and extensive hydrogen-bond and hydrophobic contact networks at key pocket residues. Both peptides were synthesized via Fmoc-based solid-phase assembly, macrocyclized under dilute conditions, purified by RP-HPLC to >95% purity, and structurally confirmed by ESI-MS (calcd/obs: A14, 757.89 Da / $[M+H]^+$ 761–762; A21, 762.87 Da / $[M+H]^+$ 762). Antiproliferative activity evaluated using the MTT assay against luminal T-47D and TNBC MDA-MB-231 cells showed that A21 was the most potent analog, with IC_{50} values of 387.99 ± 10.2 µg/mL (T-47D) and 143.15 ± 6.4 µg/mL (MDA-MB-231), outperforming A14 (710.28 ± 12.4 µg/mL and 220.05 ± 8.6 µg/mL, respectively). Both peptides demonstrated preferential cytotoxicity toward the TNBC subtype, with A21 offering a favorable balance of potency and subtype selectivity. Collectively, these findings validate a docking-led design pipeline for cyclosenegalin-based cyclic peptides and identify A21 as a tractable lead for further optimization, mechanistic studies focused on EGFR/NF-κB pathway modulation, and future *in vivo* investigations.

* Corresponding author: Sodik, Jajang Japar
✉ E-mail: jajang.japar@bku.ac.id

GRAPHICAL ABSTRACT

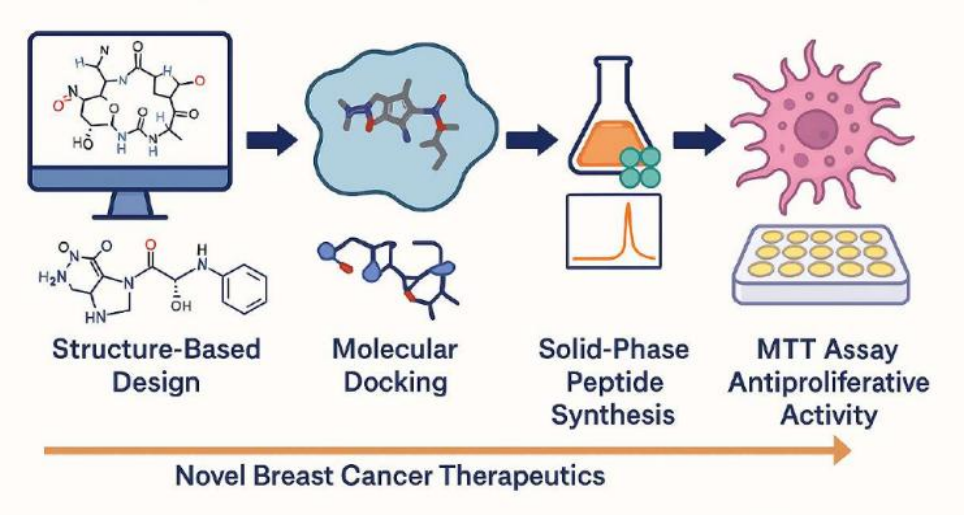

Introduction

Breast cancer is the most frequently diagnosed malignancy in women worldwide [1]. It contributes substantially to morbidity and mortality across income settings [2]. Incidence has risen with population aging, growth, and better detection [1]. Mortality patterns vary by region because access to care is uneven [3]. Screening programs shift the stage of diagnosis toward earlier disease [4]. Lifestyle exposures and reproductive history modulate population risk. Genetic predisposition explains a minority but clinically important fraction. Urbanization and dietary change correlate with increasing incidence in many countries [5]. Public awareness campaigns help, but diagnostic delays persist [6]. Health system capacity shapes the timeliness of confirmation and treatment [7]. Survival correlates strongly with stage, biology, and treatment quality. Socioeconomic and geographic disparities remain pronounced within nations. The economic burden includes direct costs and productivity losses. Advances in therapy have improved outcomes for some patients. Nevertheless, benefits are not uniformly distributed or accessible [8]. Global projections indicate a continuing increase in case numbers [1]. This trajectory will strain oncology workforces and infrastructure. These realities underscore the need for scalable, effective, and equitable interventions [1].

Breast cancer comprises biologically distinct subtypes with divergent behaviors [9]. Luminal tumors express estrogen receptors and often progesterone receptors. These cancers are driven by hormone signaling circuitry [10]. Endocrine therapy is the therapeutic backbone for luminal disease. Targeted agents like CDK4/6 or PI3K inhibitors can extend control in selected cases [11,12]. HER2-positive disease constitutes another tractable subtype with antibody-based regimens. Triple-negative breast cancer lacks ER, PR, and HER2 expression by standard assays [13]. TNBC typically presents aggressively with high proliferative indices [14]. Relapse occurs earlier and more frequently than in other subtypes. Cytotoxic chemotherapy remains the principal systemic option for TNBC [15]. Immunotherapy benefits subsets defined by PD-L1 status or tumor inflammation [16]. PARP inhibition aids patients with homologous recombination deficiency [17]. Despite these tools, durable responses are still uncommon in TNBC [18]. Resistance mechanisms

and intratumoral heterogeneity complicate management. By contrast, many luminal tumors achieve prolonged control with endocrine strategies [19]. Toxicity profiles and quality-of-life considerations differ across subtypes [20]. These contrasts highlight an unmet need for TNBC-tailored agents [21]. A rational peptide-based approach directly addresses several of these gaps [22].

Cyclosenegalin is a cyclic peptide reported from Annona species [23]. Its macrocyclic architecture confers conformational rigidity and proteolytic resilience. β-turn elements stabilize conformations thought to be bioactive [24]. Natural macrocycles often display enhanced target engagement compared to linear analogs [25]. Native cyclosenegalin shows moderate cytotoxicity in select cancer cell models. Moderate baseline activity is valuable as a starting scaffold for optimization. The cyclic topology supports side-chain diversification at multiple positions. Strategic substitutions can tune hydrophobicity, polarity, and charge. Backbone N-methylation may improve permeability and protease resistance. D-amino acids incorporation can increase serum stability without large penalties [23]. Lipidation can enhance membrane interaction when the mechanism warrants it [26]. Aromatic augmentation can strengthen π-stacking within protein clefts [27]. Conformational locking through lactam bridges can reduce entropic costs on binding [28]. Macrocycle size modulation can reshape the bioactive conformer ensemble [29]. For breast cancer, disrupting protein–protein interfaces is a promising tactic [30]. Cyclosenegalin derivatives can be engineered to target such interfaces selectively. Preliminary structure–activity concepts, therefore, justify focused exploration in TNBC. These attributes position cyclosenegalin as a credible lead for breast cancer-oriented development [22].

Solid-phase peptide synthesis can efficiently construct cyclosenegalin-derived sequences [24]. The Fmoc strategy enables iterative elongation under mild base conditions. Synthesis starts by loading the first amino acid onto a suitable resin. Activating agents such as HBTU or HATU promote amide bond formation rapidly. Each coupling is followed by Fmoc removal to reveal the next nucleophilic amine [31]. Orthogonal side-chain protections preserve reactive functionalities during assembly. Difficult couplings can be addressed with double couplings or extended times. Pseudoproline and backbone-protection tactics may mitigate aggregation on resin. After chain completion, on-resin modifications can introduce handles or constraints [32]. Macrocyclization may proceed on resin or in dilute solution to favor intramolecular closure. Head-to-tail cyclization establishes the core ring of the scaffold. Side-chain-to-side-chain lactam bridges can further constrain conformation if desired. Global deprotection and cleavage liberate the peptide from the resin [33,34]. Crude products are subjected to preparative reverse-phase HPLC to achieve high purity [35]. Analytical LC-MS confirms molecular mass and purity profiles [36]. High-resolution mass spectrometry refines identity assignments where needed. Circular dichroism and NMR can assess secondary structure and conformational bias [37]. These steps collectively deliver well-characterized analogs ready for biological testing [22].

Computational design will prioritize analogs to accelerate discovery and reduce costs [38]. Target prediction tools will nominate protein partners relevant to TNBC biology [39]. Pharmacophore modeling will define spatial arrangements essential for binding. Molecular docking will evaluate pose complementarity within prioritized targets [40]. Consensus scoring and rescoring will estimate relative binding propensities. Molecular dynamics simulations will probe complex stability in explicit solvent. MM-PBSA or related free energy approximations will rank candidates for synthesis. QSAR models will relate descriptors to predicted or observed activities. Multi-parameter

optimization will balance potency, selectivity, and developability. In silico ADME flags will guide modifications that improve exposure and stability. Top designs will advance to synthesis for experimental confirmation. Cytotoxicity testing will be performed in representative triple-negative cell lines. Mechanistic assays will interrogate apoptosis, cell cycle effects, and pathway modulation. Stability and permeability assessments will support early triage of developability. A comparative analysis will benchmark analogs against the parent cyclosenegalin. Iterative design–make–test–analyze cycles will efficiently refine hypotheses. Integrated datasets will inform clear go or no-go decisions for each series. The overarching aim is to deliver selective, potent, and safer peptide candidates tailored to TNBC.

Materials and Methods

Structural design and frequency optimization

Table 1 shows the parent cyclosenegalin A scaffold used as the template for derivative design, and lists the full analog panel (A1–A29) in 1-letter and 3-letter codes with substituted residues highlighted. All structures were first drawn in ChemDraw (CDX/CDXML), then exported as MOL/SDF and converted to 3D in Chem3D to generate reasonable starting geometries [41]. Each peptide was energy-minimized with MM2 to remove bad contacts, followed by a short conformational search (200–500 steps; RMS gradient ≤ 0.01). Quantum-mechanical optimization and frequency analysis were performed in Gaussian using the DFT B3LYP/3-21G level (*i.e.,* "B3LYP/3-21G" for geometry + frequencies) to obtain fully optimized minima; no imaginary frequencies (NIMAG = 0) were permitted; otherwise, the structure was re-optimized. From the frequency jobs, we extracted thermochemical quantities (electronic + thermal free energy, enthalpy, and entropy) to compare relative stability. For descriptors, HOMO/LUMO energies (ΔE = ELUMO–EHOMO), dipole moments, and molecular electrostatic potential (MEP/ESP) maps were computed to identify H-bond donor/acceptor hotspots and regions of electrostatic complementarity. To approximate aqueous conditions, single-point PCM(H_2O) calculations were performed on the gas-phase minima (B3LYP/6-31G(d,p)) to refine relative energies without changing the optimized geometries. The lowest-energy conformer per analog that satisfied NIMAG = 0 and exhibited favorable electronic descriptors was retained for docking. Final ligand files were exported as PDB and converted to PDBQT (AutoDockTools/OpenBabel) with Gasteiger charges and curated rotatable bonds; protonation states were assigned for pH ~7.4. This workflow (ChemDraw → Chem3D → MM2 → Gaussian B3LYP/3-21G (freq) → PCM(H_2O) single-point → PDB/PDBQT) provided energetically minimized and electronically characterized peptide models ready for receptor docking [42].

Molecular docking

Optimized peptide structures were docked against four breast cancer–relevant targets using AutoDock Vina (via PyRx 0.8): ERα (PDB: 3ERT) [43], PR (PDB: 2OVH) [44], EGFR tyrosine kinase (PDB: 2ITY) [45], and the IκBα/NF-κB complex (PDB: 1NFI) [46]. Receptors were prepared by removing crystallographic waters and nonessential heteroatoms, adding polar hydrogens, and assigning Kollman charges; missing side chains were repaired where needed. Co-crystallized ligands in each PDB entry defined the binding site centroid, and grid boxes were expanded to encompass the orthosteric pocket and adjacent subpockets fully. Ligands (A14, A21) were protonated at pH ~7.4, assigned Gasteiger charges, and converted to PDBQT with curated rotatable bonds.

Table 1. Amino acid sequences and substituted residues of cyclosenegalin-derived peptide analogs

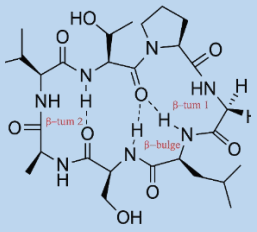

Cyclosenegalin A (PGLSAVT → Pro–Gly–Leu–Ser–Ala–Val–Thr)

Peptide analogs	Sequence (1-Letter code)	Sequence (3-Letter code)
Cyclosenegaline A1	PGKSAVT	Pro–Gly–Lys–Ser–Ala–Val–Thr
Cyclosenegaline A2	PGWSAVT	Pro–Gly–Trp–Ser–Ala–Val–Thr
Cyclosenegaline A3	PGYSAVT	Pro–Gly–Tyr–Ser–Ala–Val–Thr
Cyclosenegaline A4	PGRSAVT	Pro–Gly–Arg–Ser–Ala–Val–Thr
Cyclosenegaline A5	PGFSAVT	Pro–Gly–Phe–Ser–Ala–Val–Thr
Cyclosenegaline A6	PGLKAVT	Pro–Gly–Leu–Lys–Ala–Val–Thr
Cyclosenegaline A7	PGLYAVT	Pro–Gly–Leu–Tyr–Ala–Val–Thr
Cyclosenegaline A8	PGLHAVT	Pro–Gly–Leu–His–Ala–Val–Thr
Cyclosenegaline A9	PGLRAVT	Pro–Gly–Leu–Arg–Ala–Val–Thr
Cyclosenegaline A10	PGKKAVT	Pro–Gly–Lys–Lys–Ala–Val–Thr
Cyclosenegaline A11	PGKYAVT	Pro–Gly–Lys–Tyr–Ala–Val–Thr
Cyclosenegaline A12	PGKHAVT	Pro–Gly–Lys–His–Ala–Val–Thr
Cyclosenegaline A13	PGKRAVT	Pro–Gly–Lys–Arg–Ala–Val–Thr
Cyclosenegaline A14	PGWKAVT	Pro–Gly–Trp–Lys–Ala–Val–Thr
Cyclosenegaline A15	PGWYAVT	Pro–Gly–Trp–Tyr–Ala–Val–Thr
Cyclosenegaline A16	PGWHAVT	Pro–Gly–Trp–His–Ala–Val–Thr
Cyclosenegaline A17	PGWRAVT	Pro–Gly–Trp–Arg–Ala–Val–Thr
Cyclosenegaline A18	PGYKAVT	Pro–Gly–Tyr–Lys–Ala–Val–Thr
Cyclosenegaline A19	PGYYAVT	Pro–Gly–Tyr–Tyr–Ala–Val–Thr
Cyclosenegaline A20	PGYHAVT	Pro–Gly–Tyr–His–Ala–Val–Thr
Cyclosenegaline A21	PGYRAVT	Pro–Gly–Tyr–Arg–Ala–Val–Thr
Cyclosenegaline A22	PGRKAVT	Pro–Gly–Arg–Lys–Ala–Val–Thr
Cyclosenegaline A23	PGRYAVT	Pro–Gly–Arg–Tyr–Ala–Val–Thr
Cyclosenegaline A24	PGRHAVT	Pro–Gly–Arg–His–Ala–Val–Thr
Cyclosenegaline A25	PGRRAVT	Pro–Gly–Arg–Arg–Ala–Val–Thr
Cyclosenegaline A26	PGFKAVT	Pro–Gly–Phe–Lys–Ala–Val–Thr
Cyclosenegaline A27	PGFYAVT	Pro–Gly–Phe–Tyr–Ala–Val–Thr
Cyclosenegaline A28	PGFHAVT	Pro–Gly–Phe–His–Ala–Val–Thr
Cyclosenegaline A29	PGFRAVT	Pro–Gly–Phe–Arg–Ala–Val–Thr

Vina ran using exhaustiveness 8–16, num_modes 10, and an energy_range 3–5 kcal/mol; each receptor–ligand pair was docked in triplicate to assess reproducibility. Poses were ranked by binding free energy (ΔG, kcal/mol) and retained when the top cluster showed RMSD < 2.0 Å across replicates Noncovalent contacts (hydrogen bonds, salt bridges, π–π/π-alkyl, and hydrophobics) were analyzed in Discovery Studio Visualizer and PyMOL and mapped to pharmacophoric motifs relevant to each target. Cross-target comparisons of ΔG and interaction density were used to prioritize candidates. Based on consistently low ΔG values and rich, conserved contact networks across 3ERT, 2OVH, 2ITY, and 1NFI, A14 and A21 were advanced as lead analogs for synthesis and biological testing.

Peptide synthesis (Fmoc-SPPS)

Peptides were assembled on chlorotrityl chloride (CTC) resin (loading 0.80–1.10 mmol/g; used at 0.20 mmol scale) that was swelled for 30 min in dry DCM, and then 30 min in DMF. The first residue Fmoc-Thr(tBu)-OH (3.0 equiv) was anchored with DIPEA (6.0 equiv) in DCM/DMF (1:1) for 1 h with gentle agitation, and subsequently capped with MeOH/DIPEA/DCM (8:1:1) for 10 min to quench unreacted sites. Standard cycles used 20% piperidine/DMF (v/v; 2 × 5 min) for Fmoc removal, three DMF washes (3 × 1 min), then coupling of each Fmoc-amino acid (3.0–4.0 equiv) with HBTU/Oxyma/DIPEA (3.8/3.8/6.0 equiv) in DMF for 30–60 min. Difficult steps (aromatic/cationic residues) employed double coupling or extended time (up to 90 min) and NMP co-solvent to reduce on-resin aggregation. Sequences were Thr–Val–Ala–Lys(Boc)–Trp(Boc)–Gly–Pro (A14) and Thr–Val–Ala–Arg(Pbf)–Tyr(tBu)–Gly–Pro (A21); side-chain protections were kept intact throughout assembly. Reaction progress was monitored by Kaiser (ninhydrin) and chloranil tests; any positive color after coupling triggered a repeat coupling. After chain completion, the resin was washed (DMF, DCM, MeOH) and dried, then acidic cleavage with TFA:TIS:H_2O (95:2.5:2.5, v/v/v) for 2 h released the linear peptide with side-chain deprotection. Crude filtrates were concentrated with N_2, precipitated into ice-cold diethyl ether (10× volume), centrifuged (4000 g, 10 min), washed twice with ether, and dried. Head-to-tail macrocyclization was performed at 0.5–1.0 mM (to suppress oligomerization) in DMF/DCM (1:1) using PyBOP or PyBOP/HOAt (1.2 equiv) and DIPEA (3–4 equiv) for 2–16 h at rt; completion was checked by LC-MS. Work-up used dilution with water and solid-phase extraction (C18 cartridge) prior to prep-RP-HPLC. Final purification employed C18 column (250 × 21.2 mm, 10 µm), 0.1% TFA in water (A) and ACN (B), with a linear gradient from 5 to 60% B over 30–40 min, 15–20 mL/min, and detection at 214/220/280 nm. Fractions (>95% peak purity by analytical HPLC) were pooled, lyophilized, and stored −20 °C, desiccated, until analysis and bioassay [24].

Peptide characterization

Identity was verified by ESI-MS (positive mode) using a single quadrupole or Q-TOF instrument with a capillary voltage of 3.5 kV, source 120–150 °C, desolvation 250–300 °C, and N_2 as nebulizing gas. Samples were prepared at 10–20 µM in H_2O/ACN 1:1 (0.1% formic acid) and infused at 5–10 µL/min; spectra were acquired over m/z 500–1500 with 0.2–0.5 s scans. Theoretical masses (ChemDraw) were A14 = 757.89 Da and A21 = 762.87 Da; observed ions were assigned to $[M+H]^+$ (main) and minor $[M+2H]^{2+}$/$[M+3H]^{3+}$ envelopes; Na^+/K^+ adducts were checked and, if present, removed by additional desalting. HRMS (where available) provided exact mass within ≤5 ppm error. Analytical purity was confirmed by HPLC (C18, 150 × 4.6 mm, 5 µm) with A: H_2O+0.1% TFA, B: ACN+0.1% TFA, gradient 5→60% B over 20 min, 1.0 mL/min, UV at 220 nm;

purity threshold for biological testing was ≥95% (area %). Retention times and UV traces were archived for batch traceability. Stability was assessed by re-injecting samples stored 24 h at 4 °C and 72 h at −20 °C; acceptance was <5% degradation by area. Where needed, ^{1}H-NMR (400 MHz, DMSO-d_6) was recorded to confirm backbone integrity and aromatic patterns (Trp/Tyr). All raw data (mzML/HPLC chromatograms) were processed in vendor software and exported for deposition in the repository [24].

In vitro cytotoxicity assay (MTT)

T-47D and MDA-MB-231 cells were authenticated (STR profiling) and confirmed mycoplasma-free before use. Cells were maintained in RPMI-1640 + 10% FBS + 1% penicillin–streptomycin at 37 °C, 5% CO_2, subcultured at 70–80% confluence using 0.25% trypsin-EDTA. For assays, cells were seeded in 96-well plates at 1.0×10^4 cells/well (100 µL) and allowed to attach for 16–18 h. Peptide stocks were made in sterile PBS (or minimal DMSO ≤0.5% v/v in the well; vehicle kept constant across groups) and diluted to 25, 50, 100, 200, 400, 600, 800, and 1,000 µg/mL. After 24 h exposure (optional 48 h confirmatory set), MTT (5 mg/mL) was added 10 µL/well and incubated 3–4 h until purple formazan formed. The medium was carefully removed, 100 µL of DMSO was added to dissolve the crystals, and absorbance was read at 570 nm with a 630–690 nm background correction. Each condition had n=3–6 technical replicates and ≥ 3 biological repeats on separate days; plate maps included an untreated control, a vehicle control, and an optional positive control (*e.g.,* doxorubicin at 1–5 µM) to assess assay performance. Percent viability = 100 × (A_{570} sample / A_{570} control); IC_{50} values were obtained by 4-parameter logistic (4PL) nonlinear regression in GraphPad Prism 9, constrained between 0–100%. Quality criteria included R^2 ≥ 0.95, monotonic dose–response, and CV ≤ 15% across replicates; outliers were checked by the ROUT method (Q=1%) when justified. The selectivity index (SI) was calculated as SI = IC_{50}(T-47D) / IC_{50}(MDA-MB-231) for each run and reported as the mean ± SD. Optional follow-ups (not required for IC_{50}) included trypan blue viability, Annexin V/PI apoptosis readouts, and time course at 6/12/24/48 h to verify kinetics [47].

Results

Electronic behavior and reactivity analysis of cyclosenegalin analog peptides

The quantum chemical analysis presented in Table 2 demonstrates the electronic stability, polarity, and reactivity patterns of the cyclosenegalin-derived peptide analogs. All total energy values are strongly negative, indicating that each analog is thermodynamically stable at the optimized geometry. The lowest total energy is observed for cyclosenegalin A17 (−2836.19 a.u.), followed by A19 (−2803.46 a.u.) and A21 (−2780.08 a.u.), confirming their higher electronic stability compared to earlier analogs such as A1 (−2441.40 a.u.). The progressive decrease in total energy across the series implies that specific substitutions and conformational constraints enhance molecular stability. Dipole moment values range from 4.71 D (A2) to 18.45 D (A25), reflecting significant variability in charge distribution and polarity. Analog A25 exhibits the highest dipole moment, suggesting strong polarity and potential for aqueous solubility, while analog A2 shows hydrophobic character that could improve membrane penetration. The HOMO values range from −0.068 eV to −0.130 eV, with lower values indicating greater resistance to oxidation and better electronic stability. Similarly, LUMO energies range from −0.159 eV to −0.229 eV, with lower values suggesting stronger electron affinity.

Table 2. Quantum chemical parameters of cyclosenegalin-derived peptide analogs

Peptide analogs	Parameters			
	Total energy	Dipole moment	HOMO	LUMO
Cyclosenegaline A1	-2441.40158569	5.0886	-0.07110	-0.20919
Cyclosenegaline A2	-2629.67247828	4.7158	-0.07262	-0.18519
Cyclosenegaline A3	-2573.64537962	7.8610	-0.07421	-0.20461
Cyclosenegaline A4	-2550.29817962	6.3864	-0.06793	-0.21251
Cyclosenegaline A5	-2498.84731957	6.5297	-0.07383	-0.22971
Cyclosenegaline A6	-2483.91354266	11.7743	-0.12662	-0.19857
Cyclosenegaline A7	-2616.15915005	12.4347	-0.12614	-0.20630
Cyclosenegaline A8	-2535.35928895	15.5230	-0.13042	-0.20789
Cyclosenegaline A9	-2592.81308505	12.4400	-0.12363	-0.20513
Cyclosenegaline A10	-2538.94167343	11.4457	-0.12470	-0.20576
Cyclosenegaline A11	-2671.14040520	5.9650	-0.08754	-0.20888
Cyclosenegaline A12	-2590.37998958	15.2946	-0.07751	-0.21250
Cyclosenegaline A13	-2647.84085442	11.9310	-0.12293	-0.20562
Cyclosenegaline A14	-2727.26136954	9.9361	-0.12054	-0.19109
Cyclosenegaline A15	-2859.44618425	9.4223	-0.10699	-0.20761
Cyclosenegaline A16	-2778.62313330	6.9734	-0.10142	-0.20825
Cyclosenegaline A17	-2836.18469389	15.0052	-0.11319	-0.17433
Cyclosenegaline A18	-2671.18777952	11.7321	-0.12692	-0.20037
Cyclosenegaline A19	-2803.46309134	14.7677	-0.12620	-0.19700
Cyclosenegaline A20	-2722.66109318	17.7883	-0.13003	-0.20236
Cyclosenegaline A21	-2780.08745723	12.2147	-0.12393	-0.20204
Cyclosenegaline A22	-2647.79176718	2.3173	-0.10463	-0.19520
Cyclosenegaline A23	-2780.08077058	14.2291	-0.06875	-0.19241
Cyclosenegaline A24	-2699.23979316	14.6904	-0.07230	-0.20082
Cyclosenegaline A25	-2756.74551096	18.4453	-0.12248	-0.18165
Cyclosenegaline A26	-2596.38976682	11.1251	-0.12639	-0.20091
Cyclosenegaline A27	-2728.12602405	7.8906	-0.07226	-0.15942
Cyclosenegaline A28	-2647.86269485	14.6658	-0.12176	-0.20825
Cyclosenegaline A29	-2705.28936652	11.8885	-0.12355	-0.20686

The energy gap (ΔE = LUMO–HOMO) provides insight into molecular reactivity and softness; smaller gaps correspond to higher electronic reactivity. The smallest ΔE is seen in A25 (≈ 0.059 eV), followed by A17 (≈ 0.061 eV), indicating potentially stronger intermolecular interactions with biological targets. Conversely, larger ΔE values in A5 (≈ 0.155 eV) and A1 (≈ 0.138 eV) suggest lower reactivity but higher inertness. These findings highlight how conformational tuning directly influences electronic distribution, reactivity, and stability, forming a basis for correlating quantum descriptors with biological potency.

Further examination of individual analogs reveals distinct features that can guide candidate prioritization for anticancer evaluation. Peptides A17, A25, and A8 display an optimal combination of high thermodynamic stability and low ΔE, suggesting a balanced profile of reactivity and durability suitable for enzyme binding and receptor targeting. Analog A25, with its highest dipole moment and narrowest energy gap, may interact efficiently within polar tumor microenvironments, although excessive polarity may reduce passive membrane permeability. Analog A17 shows similar electronic characteristics but a slightly lower dipole moment, potentially favoring both solubility and more balanced diffusion. Intermediate-reactivity analogs such as A8, A18, A10, and A13 exhibit ΔE values around 0.075–0.085 eV, representing a promising midpoint between chemical robustness and electronic adaptability. Analogs with large ΔE values, such as A3, A12, and A24, appear more inert and may serve as negative controls or scaffold baselines. High dipole moments in A8 (15.52 D), A20 (17.78 D), and A24 (14.69 D) indicate improved capacity for hydrogen bonding and electrostatic interactions at polar receptor sites. Conversely, highly negative HOMO energies in A8 (−0.130 eV) and A20 (−0.130 eV) suggest enhanced oxidative stability favorable for biological environments. LUMO minima in A5 (−0.229 eV) and A4 (−0.212 eV) reflect strong electron-acceptor tendencies, possibly influencing π–π or charge-transfer interactions with amino acid residues. Integrating these descriptors suggests that analogs A17, A25, A8, and A18 should be prioritized for synthesis and docking studies, while A3, A12, and A24 can be retained as inert comparators. Altogether, these quantum insights form a rational foundation for linking molecular electronics to structure–activity relationships in the design of potent and selective cyclosenegalin-based anticancer peptides.

Comparative docking evaluation of cyclosenegalin analogs across multiple breast cancer targets

The docking results for hormonal receptors reveal a wide dispersion of affinities across the cyclosenegalin analog series (Table 3). For ERα, scores span approximately −6.1 to −10.1 kcal/mol, indicating variable stability of the peptide–receptor complexes. Cyclosenegalin A14 shows the strongest ERα binding affinity at −10.1 kcal/mol, making it a top candidate for modulation of the estrogen pathway. Analog A2 follows closely with −9.2 kcal/mol, suggesting favorable complementarity to the ERα ligand-binding pocket. A21 and A17 also perform well with −9.1 and −9.0 kcal/mol, respectively, reinforcing the trend that specific substitutions enhance receptor engagement. In contrast, A1, A5, and A10 cluster near −7 kcal/mol, consistent with weaker stabilization of the bound pose. The spread in ERα scores likely reflects differences in hydrophobic contact networks and hydrogen bond topology elicited by side-chain changes. For PR, the majority of analogs fall between −7.0 and −9.3 kcal/mol, suggesting generally moderate to strong interactions. A21 achieves the best PR affinity of −9.3 kcal/mol, again highlighting that scaffold features which enable ERα recognition can also favor PR binding.

Table 3. Binding affinities of cyclosenegalin-derived peptide analogs against selected breast cancer targets

Peptide analogs	Binding affinity (kcal/mol)			
	Estrogen receptor alpha	Progesterone receptor	EGFR tyrosine kinase	NF-kB / lkB-α
Cyclosenegalin A1	-7.3	-6.1	-7.3	-7.3
Cyclosenegalin A2	-9.2	-8.7	-10.9	-9.0
Cyclosenegalin A3	-8.0	-7.3	-7.9	-7.7
Cyclosenegalin A4	-7.6	-6.4	-6.6	-6.8
Cyclosenegalin A5	-7.2	-7.3	-8.2	-7.1
Cyclosenegalin A6	-7.4	-7.1	-7.4	-6.3
Cyclosenegalin A7	-7.9	-8.8	-8.3	-7.3
Cyclosenegalin A8	-7.4	-7.3	-7.5	-8.3
Cyclosenegalin A9	-7.9	-7.2	-7.1	-6.8
Cyclosenegalin A10	-6.1	-6.8	-7.2	-6.1
Cyclosenegalin A11	-8.2	-8.0	-7.3	-5.5
Cyclosenegalin A12	-7.0	-7.3	-6.7	-6.3
Cyclosenegalin A13	-7.1	-7.6	-6.9	-6.8
Cyclosenegalin A14	-10.1	-9.2	-9.6	-9.1
Cyclosenegalin A15	-7.8	-7.9	-8.8	-8.9
Cyclosenegalin A16	-7.5	-7.8	-8.0	-8.4
Cyclosenegalin A17	-9.0	-8.7	-8.1	-7.9
Cyclosenegalin A18	-8.0	-7.7	-7.8	-7.6
Cyclosenegalin A19	-7.7	-8.8	-8.0	-9.2
Cyclosenegalin A20	-7.5	-8.7	-8.2	-6.9
Cyclosenegalin A21	-9.1	-9.3	-10.4	-9.2
Cyclosenegalin A22	-7.6	-7.3	-8.1	-7.2
Cyclosenegalin A23	-7.4	-8.0	-7.3	-7.5
Cyclosenegalin A24	-6.8	-7.9	-7.4	-7.3
Cyclosenegalin A25	-7.8	-7.0	-7.4	-7.3
Cyclosenegalin A26	-7.0	-7.4	-7.4	-8.6
Cyclosenegalin A27	-8.1	-8.3	-8.8	-8.5
Cyclosenegalin A28	-7.3	-8.3	-8.1	-6.9
Cyclosenegalin A29	-7.6	-8.6	-8.3	-7.2

A14 ranks second at −9.2 kcal/mol, providing cross-validation of its dual hormonal targeting potential. Analogs with mid-range PR scores, such as A12 and A23 around −7.3 to −8.0 kcal/mol, may still contribute meaningfully to combination designs. The apparent concordance between ERα and PR performance suggests a shared pharmacophore motif within the macrocycle. Such dual engagement could reduce compensatory signaling that often undermines single-receptor therapies. However, the polarity and size of the peptides imply that receptor selectivity will also depend on the local microenvironment and induced-fit effects. In general, the hormonal receptor panel nominates A14, A2, A21, and A17 as priority analogs for deeper structural and biophysical evaluation.

The kinase and inflammatory targets expand the activity landscape and further differentiate the analogs. Against EGFR tyrosine kinase, A2 records the lowest docking energy at −10.9 kcal/mol, consistent with a tightly packed ATP-site pose. A21 follows with −10.4 kcal/mol, while A14 posts −9.6 kcal/mol, together defining a high-affinity cluster. Several analogs, including A7, A15, A16, and A20, fall within the −8.0 to −8.8 kcal/mol range, suggesting a yet more moderate level of engagement. These values imply that selective steric and electrostatic tuning within the macrocycle can modulate the complementarity of the kinase pocket. For NF-κB/IκB-α, A19 and A21 exhibit the most favorable scores at −9.2 kcal/mol, with A14 close behind at −9.1 kcal/mol. This profile is consistent with the potential disruption of protein–protein interactions governing transcriptional activation. Analog A8 shows −8.3 kcal/mol on this axis, suggesting additional anti-inflammatory synergy candidates. Cross-target inspection reveals that A14 and A21 deliver consistently strong binding across ERα, PR, EGFR, and NF-κB/IκB-α. Such multi-target behavior is attractive in TNBC contexts, where pathway redundancy drives resistance. Conversely, analogs with modest or uneven performance can serve as comparators to delineate structure–affinity rules. Integrating these results with quantum descriptors and dipole moments will enable more reliable ranking through multi-parameter optimization. The immediate next step is to validate poses through molecular dynamics and to compute per-residue energy decompositions. Parallel *in vitro* assays should test antiproliferative effects, apoptosis markers, and pathway readouts to connect docking to phenotype. Taken together, the dataset supports prioritization of A14, A21, A2, and A19 as lead scaffolds for iterative design, synthesis, and biological evaluation.

Molecular interaction mechanisms of cyclosenegalin-derived peptides with breast cancer receptors

The interaction mapping summarized in Table 4 highlights distinct binding patterns between cyclosenegalin analogs and key breast cancer receptor targets, revealing how specific residue interactions contribute to molecular stability and target specificity. For the Estrogen Receptor Alpha (ERα), the native ligand predominantly interacts through hydrogen bonds with residues ARG394, GLU353, LEU387, THR347, and ASP351, which are canonical anchoring sites in the hormone-binding pocket. Additional hydrophobic contacts with LEU346, MET388, and MET421 provide secondary stabilization via alkyl and π-alkyl interactions. In contrast, cyclosenegalin A14 demonstrates an optimized network involving six hydrogen bonds with THR347, VAL533, LYS531, ASP351, PRO535, and CYS530, supplemented by hydrophobic π-alkyl interactions with VAL533 and LEU536. These interactions mimic several native binding motifs, particularly at THR347 and ASP351, implying bioisosteric complementarity between the analog and the receptor's polar core.

Table 4. Interaction profile of cyclosenegalin-derived peptide analogs with selected breast cancer targets

Target receptors	Peptide analogs	Interaction	Category	Type of interaction
Estrogen receptor alpha	Native ligand	A:ARG394	Hydrogen bond	Conventional hydrogen bond
		A:GLU353	Hydrogen bond	Conventional hydrogen bond
		A:LEU387	Hydrogen bond	Conventional hydrogen bond
		A:THR347	Hydrogen bond	Carbon hydrogen bond
		A:ASP351	Hydrogen bond	Carbon hydrogen bond
		A:LEU346	Hydrophobic	Amide-Pi stacked
		A:LEU346	Hydrophobic	Alkyl
		A:MET388	Hydrophobic	Alkyl
		A:MET421	Hydrophobic	Alkyl
		A:ALA350	Hydrophobic	Pi-Alkyl
		A:LEU387	Hydrophobic	Pi-Alkyl
		A:LEU391	Hydrophobic	Pi-Alkyl
		A:LEU346	Hydrophobic	Pi-Alkyl
		A:ALA350	Hydrophobic	Pi-Alkyl
		A:LEU525	Hydrophobic	Pi-Alkyl
		A:MET421	Hydrophobic	Pi-Alkyl
		A:LEU525	Hydrophobic	Pi-Alkyl
	A14	A:THR347	Hydrogen bond	Conventional hydrogen bond
		A:VAL533	Hydrogen bond	Conventional hydrogen bond
		A:LYS531	Hydrogen bond	Conventional hydrogen bond
		A:ASP351	Hydrogen bond	Conventional hydrogen bond
		A:PRO535	Hydrogen bond	Carbon hydrogen bond
		A:CYS530	Hydrogen bond	Carbon hydrogen bond
		A:VAL533	Hydrophobic	Pi-Alkyl
		A:LEU536	Hydrophobic	Pi-Alkyl
	A21	A:CYS381	Hydrogen bond	Conventional hydrogen bond
		A:CYS381	Hydrogen bond	Conventional hydrogen bond
		A:SER518	Hydrogen bond	Conventional hydrogen bond
		A:CYS530	Hydrogen bond	Conventional hydrogen bond
		A:VAL534	Hydrogen bond	Conventional hydrogen bond
		A:ASP351	Hydrogen bond	Conventional hydrogen bond
		A:LYS531	Hydrogen bond	Conventional hydrogen bond
		A:VAL533	Hydrogen bond	Conventional hydrogen bond
		A:CYS530	Hydrogen bond	Conventional hydrogen bond
		A:ASN519	Hydrogen bond	Carbon hydrogen bond
		A:LEU536	Hydrogen bond	Carbon hydrogen bond
		A:MET522	Hydrophobic	Alkyl
		A:LEU525	Hydrophobic	Alkyl
Progesterone receptor	Native ligand	A:GLN725	Hydrogen bond	Conventional hydrogen bond
		A:ARG766	Hydrogen bond	Conventional hydrogen bond

Target receptors	Peptide analogs	Interaction	Category	Type of interaction
EGFR tyrosine kinase	A14	A:PHE794	Hydrophobic	Pi-Sigma
		A:GLY722	Hydrophobic	Amide-Pi stacked
		A:LEU797	Hydrophobic	Alkyl
		A:CYS891	Hydrophobic	Alkyl
		A:ASN719	Hydrogen bond	Conventional hydrogen bond
		A:CYS891	Hydrogen bond	Conventional hydrogen bond
		A:CYS891	Hydrogen bond	Conventional hydrogen bond
		A:SER898	Hydrogen bond	Conventional hydrogen bond
		A:SER712	Hydrogen bond	Conventional hydrogen bond
		A:THR716	Hydrogen bond	Conventional hydrogen bond
		A:ASN719	Hydrogen bond	Conventional hydrogen bond
		A:GLU723	Hydrogen bond	Conventional hydrogen bond
		A:ASN719	Hydrogen bond	Carbon hydrogen bond
		A:PHE895	Hydrophobic	Pi-Pi stacked
		A:LEU715	Hydrophobic	Alkyl
		A:MET801	Hydrophobic	Alkyl
		A:VAL912	Hydrophobic	Pi-Alkyl
	A21	A:ASN719	Hydrogen bond	Conventional hydrogen bond
		A:SER898	Hydrogen bond	Conventional hydrogen bond
		A:ASN719	Hydrogen bond	Conventional hydrogen bond
		A:MET759	Hydrogen bond	Conventional hydrogen bond
		A:ASN719	Hydrogen bond	Conventional hydrogen bond
		A:PHE895	Hydrogen bond	Carbon hydrogen bond
		A:LEU718	Hydrophobic	Alkyl
		A:CYS891	Hydrophobic	Alkyl
	Native ligand	A:PHE723	Hydrogen bond	Conventional hydrogen bond
		A:GLY724	Hydrogen bond	Conventional hydrogen bond
		A:THR854	Hydrogen bond	Conventional hydrogen bond
		A:THR790	Hydrogen bond	Pi-Donor hydrogen bond
		A:THR790	Hydrophobic	Pi-Sigma
		A:LEU844	Hydrophobic	Pi-Sigma
		A:LEU844	Hydrophobic	Pi-Sigma
		A:MET766	Hydrophobic	Alkyl
		A:ALA743	Hydrophobic	Pi-Alkyl
		A:LEU844	Hydrophobic	Pi-Alkyl
		A:ALA743	Hydrophobic	Pi-Alkyl
		A:CYS775	Hydrophobic	Pi-Alkyl
		A:LEU844	Hydrophobic	Pi-Alkyl
	A14	A:ASP855	Hydrogen bond;electrostatic	Salt bridge;attractive charge
		A:LYS745	Hydrogen bond	Conventional hydrogen bond
		A:CYS797	Hydrogen bond	Conventional hydrogen bond

Target receptors	Peptide analogs	Interaction	Category	Type of interaction
NF-kB / lkB-α	Native ligand	A:CYS797	Hydrogen bond	Conventional hydrogen bond
		A:ASP855	Hydrogen bond	Conventional hydrogen bond
		A:GLU762	Hydrogen bond	Conventional hydrogen bond
		A:ASP855	Hydrogen bond	Conventional hydrogen bond
		A:ARG841	Hydrogen bond	Conventional hydrogen bond
		A:MET793	Hydrogen bond	Conventional hydrogen bond
		A:PHE723	Hydrophobic	Pi-Pi stacked
		A:LEU747	Hydrophobic	Pi-Alkyl
	A21	A:GLU758	Electrostatic	Attractive charge
		A:ASP855	Electrostatic	Attractive charge
		A:MET793	Hydrogen bond	Conventional hydrogen bond
		A:MET793	Hydrogen bond	Conventional hydrogen bond
		A:ASP855	Hydrogen bond	Conventional hydrogen bond
		A:GLU762	Hydrogen bond	Conventional hydrogen bond
		A:SER720	Hydrogen bond	Conventional hydrogen bond
		A:SER720	Hydrogen bond	Conventional hydrogen bond
		A:GLY721	Hydrogen bond	Conventional hydrogen bond
		A:GLY857	Hydrogen bond	Carbon hydrogen bond
		A:ASN842	Hydrogen bond	Carbon hydrogen bond
		A:GLU758	Hydrogen bond	Carbon hydrogen bond
		A:VAL726	Hydrophobic	Alkyl
		A:ALA743	Hydrophobic	Alkyl
		A:ALA743	Hydrophobic	Alkyl
		A:LYS745	Hydrophobic	Alkyl
		A:LEU718	Hydrophobic	Alkyl
		A:LEU792	Hydrophobic	Alkyl
		A:LEU844	Hydrophobic	Alkyl
		A:ARG408	Hydrogen bond	Conventional hydrogen bond
		A:LEU472	Hydrogen bond	Conventional hydrogen bond
		A:PHE535	Hydrogen bond	Conventional hydrogen bond
		A:GLU470	Hydrogen bond	Conventional hydrogen bond
		A:GLU440	Hydrogen bond	Conventional hydrogen bond
		A:VAL414	Hydrophobic	Pi-Sigma
		A:VAL414	Hydrophobic	Pi-Sigma
		A:VAL414	Hydrophobic	Alkyl
		A:LYS429	Hydrophobic	Alkyl
		A:CYS533	Hydrophobic	Alkyl
		A:LEU522	Hydrophobic	Pi-Alkyl
		A:CYS533	Hydrophobic	Pi-Alkyl
		A:VAL414	Hydrophobic	Pi-Alkyl
		A:ALA427	Hydrophobic	Pi-Alkyl
		A:MET469	Hydrophobic	Pi-Alkyl
		A:LEU522	Hydrophobic	Pi-Alkyl

Target receptors	Peptide analogs	Interaction	Category	Type of interaction
	A14	A:HIS594	Hydrogen bond	Conventional hydrogen bond
		A:THR597	Hydrogen bond	Conventional hydrogen bond
		A:ASP519	Hydrogen bond	Conventional hydrogen bond
		A:GLY478	Hydrogen bond	Conventional hydrogen bond
		A:GLY407	Hydrogen bond	Conventional hydrogen bond
		A:GLY409	Hydrogen bond	Carbon hydrogen bond
		A:HIS588	Hydrogen bond	Carbon hydrogen bond
		A:SER410	Hydrogen bond	Carbon hydrogen bond
		A:LEU522	Hydrophobic	Alkyl
	A21	A:THR597	Hydrogen bond	Conventional hydrogen bond
		A:ASP519	Hydrogen bond	Conventional hydrogen bond
		A:SER476	Hydrogen bond	Conventional hydrogen bond
		A:CYS533	Hydrogen bond	Conventional hydrogen bond
		A:ASN520	Hydrogen bond	Conventional hydrogen bond
		A:ASP534	Hydrogen bond	Conventional hydrogen bond
		A:ASP534	Hydrogen bond	Carbon hydrogen bond
		A:HIS594	Electrostatic	Pi-cation
		A:ARG408	Hydrophobic	Alkyl
		A:VAL414	Hydrophobic	Alkyl
		A:CYS533	Hydrophobic	Alkyl
		A:PRO675	Hydrophobic	Alkyl

The dual presence of hydrogen and hydrophobic contacts in A14 indicates a favorable balance between affinity and conformational flexibility, contributing to the strong docking energy observed earlier (−10.1 kcal/mol). Moreover, cyclosenegalin A21 forms an even more extensive hydrogen-bonding network, engaging residues CYS381, SER518, CYS530, VAL534, ASP351, and LYS531, along with hydrophobic stabilizations at LEU525 and MET522. The dense hydrogen bond cluster of A21 enhances its electrostatic anchoring and contributes to consistent binding energy (−9.1 kcal/mol). The overall comparison suggests that A14 and A21 exhibit improved polar complementarity and hydrophobic packing relative to the native ligand, reinforcing their potential as potent ERα modulators that can disrupt estrogen-driven proliferation in breast cancer cells. For the progesterone receptor, the native ligand forms two principal hydrogen bonds with GLN725 and ARG766, complemented by hydrophobic π-stacking with PHE794 and additional alkyl contacts at LEU797 and CYS891. In contrast, cyclosenegalin A14 exhibits a broader network of nine hydrogen bonds involving ASN719, CYS891, SER898, SER712, THR716, GLU723, and ASN719, indicating a tighter polar engagement across the ligand-binding cavity. This enhanced hydrogen-bond saturation suggests greater enthalpic stabilization and potentially stronger antagonistic behavior. A14 also forms π-π stacking with PHE895 and alkyl interactions with LEU715 and VAL912, underscoring its amphiphilic adaptability. Meanwhile, cyclosenegalin A21 retains several conserved hydrogen-bond contacts with ASN719, SER898, MET759, and PHE895, while maintaining hydrophobic stabilization at LEU718 and CYS891. The overlap between binding residues such as ASN719 and CYS891 and those of the native ligand

indicates a high structural mimicry of endogenous hormones. For EGFR tyrosine kinase, both analogs maintain electrostatic and hydrogen bond interactions with critical residues ASP855, LYS745, and CYS797, which are key determinants for ATP-binding inhibition. A21 also introduces salt-bridge interactions, suggesting increased binding strength through charge complementarity. Finally, within NF-κB/IκB-α, analogs A14 and A21 engage numerous hydrogen bonds with ASP519, GLY478, THR597, and HIS594, paralleled by hydrophobic stabilization through VAL414 and LEU522. These residue-specific interactions imply that cyclosenegalin analogs act via multipoint anchoring, simultaneously occupying polar and nonpolar subsites. Collectively, these findings confirm that A14 and A21 reproduce or exceed the native ligand's binding characteristics across all receptor targets, establishing them as multifunctional candidates for peptide-based breast cancer therapy.

Rational selection and synthetic assembly of cyclosenegalin-derived peptides

These peptide analogs were selected for synthesis because prior docking consistently ranked A14 and A21 among the top binders against ERα, PR, EGFR, and NF-κB/IκB-α. The docking poses revealed dense hydrogen bond networks and complementary hydrophobic packing in both analogs. Residue-level contact maps suggested that a basic side chain and a single aromatic ring were key contributors to affinity. Those insights informed the decision to retain a conserved Thr-Val-Ala scaffold for physicochemical balance. The sequence plan then varied only the cationic and aromatic residues to test binding hypotheses. Fmoc-based solid-phase peptide synthesis (SPPS) was chosen to control sequence fidelity and side chain protection. Chlorotrityl chloride resin provided an acid-labile anchor compatible with mild global cleavage. Uronium-mediated couplings with DIPEA were used to form amide bonds efficiently at each elongation step. Routine Fmoc deprotection with piperidine exposed the incoming amine for the next coupling. Aggregation risks were mitigated through resin swelling and, if needed, double coupling. Orthogonal protections (Boc, Pbf, and tBu) safeguarded reactive side chains during assembly. After chain completion, TFA cleavage simultaneously released the peptide and removed protections. Preparative RP-HPLC purified the crude linear products to obtain high chemical purity. Macrocyclization was performed under dilute conditions to favor intramolecular closure over oligomerization.

The A14 synthesis begins on chlorotrityl chloride resin that is briefly activated, followed by loading Fmoc-Thr(tBu)-OH with DIPEA in DMF to create an acid-labile C-terminal anchor. Couplings are mediated by HBTU/Oxyma/DIPEA to minimize racemization while maintaining rapid acylation kinetics. The Kaiser test monitors reaction progress at each cycle, and when aromatic residues are involved, the chloranil test is used. Figure 1 summarizes the residue order, showing that after 20% piperidine in DMF removes Fmoc, the chain is extended with Fmoc-Val-OH to build a compact, early hydrophobic core. Fmoc-Ala-OH is then inserted as a small spacer that reduces steric congestion and preserves predictable backbone geometry. The cationic position is established with Fmoc-Lys(Boc)-OH, with the Boc group retained to suppress ε-amine side reactions during subsequent couplings.

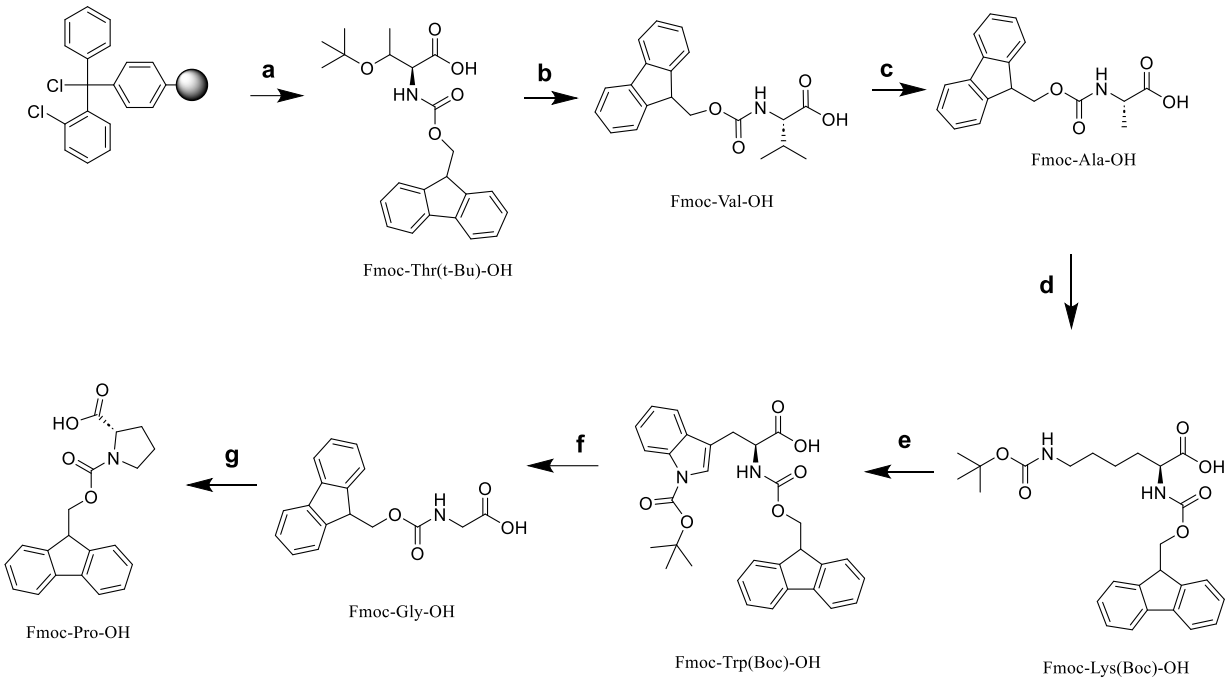

Figure 1. Synthetic scheme of cyclosenegalin A14-derived peptide using Fmoc-based SPPS method

The aromatic block employs Fmoc-Trp(Boc)-OH to introduce an indole ring capable of π–π stacking and edge-to-face contacts in receptor clefts. Fmoc-Gly-OH is incorporated next to provide local flexibility that facilitates low-entropy macrocyclization later. Fmoc-Pro-OH caps the linear assembly, biasing the chain toward a turn that preorganizes the macrocycle for binding. Difficult couplings are addressed with double-coupling protocols or extended reaction times to drive conversions toward completion. Resin swelling with DMF/DCM mixtures is used to mitigate on-resin aggregation and improve diffusion of reagents. When residual free amine is detected, an acetyl "capping" step is applied to block potential deletion sequences. Global deprotection and cleavage proceed with TFA:TIS:H2O (95:2.5:2.5) at ambient temperature to remove protecting groups and release the peptide. The filtrate is concentrated, and the crude peptide is precipitated into cold diethyl ether to discard scavengers and side products. Purification by acidic RP-HPLC affords a single major fraction whose identity is confirmed by LC-MS and, when needed, HRMS, yielding an A14 precursor consistent with the lysine–tryptophan design.

The A21 assembly retains the same resin platform and activation protocol to ensure synthetic parity with the comparator analog. The chain is initiated by loading Fmoc-Thr(tBu)-OH, followed by standard Fmoc removal to expose the nucleophilic amine for the next coupling. Fmoc-Val-OH is added to reproduce the early hydrophobic module, supporting packing without compromising reactivity. Fmoc-Ala-OH serves as a steric balancer, maintaining conformational agility and a compact backbone. The sequence diverges at the cationic position with Fmoc-Arg(Pbf)-OH, introducing a guanidinium group capable of bidentate hydrogen bonding and salt-bridge formation. Pbf protection is maintained throughout the assembly and removed only at the global deprotection step to avoid undesired side reactions. The aromatic module uses Fmoc-Tyr(tBu)-OH in place of tryptophan, adding a phenolic functionality that can donate hydrogen bonds while retaining π character. Fmoc-Gly-OH is inserted to relax local strain and to enable favorable torsional sampling prior to ring closure.

Fmoc-Pro-OH terminates the linear sequence, increasing the probability of a β-turn-like conformation that facilitates macrocyclization. Each coupling step is bracketed by Fmoc removal, with Kaiser testing used to verify the consumption of the previous amine. Episodes of on-resin aggregation during arginine or tyrosine introduction are mitigated by adding NMP as a cosolvent and by extending agitation time. Global TFA:TIS:H_2O treatment simultaneously releases the peptide, removes Pbf and tBu protections, and preserves the integrity of the backbone. The crude product is precipitated, washed, and then purified by RP-HPLC until chromatographic purity criteria are met. Identity is verified by LC-MS, with rapid ^{1}H-NMR checks used when necessary to assess rotameric heterogeneity. Figure 2 corroborates that the arginine–tyrosine motif generates a more strongly cationic and hydrogen bond-rich profile than A14, aligning with the docking-derived multi-target selectivity hypothesis.

Mass spectrometric analysis of cyclosenegalin-derived peptides

Mass spectrometry analysis was performed to confirm the molecular identity of cyclosenegalin A14 and A21, synthesized through the Fmoc-based SPPS method. Electrospray ionization in positive mode (ESI+) was chosen because it is well-suited for detecting peptide-based compounds with multiple protonation sites. The theoretical molecular weights calculated in ChemDraw were 757.89 Da for A14 and 762.87 Da for A21, which were used as benchmarks for comparison with experimental spectra. The ionization of these peptides typically results in protonated molecular ions, denoted as $[M+H]^+$, along with possible doubly charged $[M+2H]^{2+}$ and triply charged $[M+3H]^{3+}$ species. The comparison between theoretical and experimental masses serves as a strong indicator of synthetic accuracy and molecular integrity. ESI-MS is particularly advantageous for this class of peptides, as it produces minimal fragmentation and allows direct detection of intact molecular ions. The

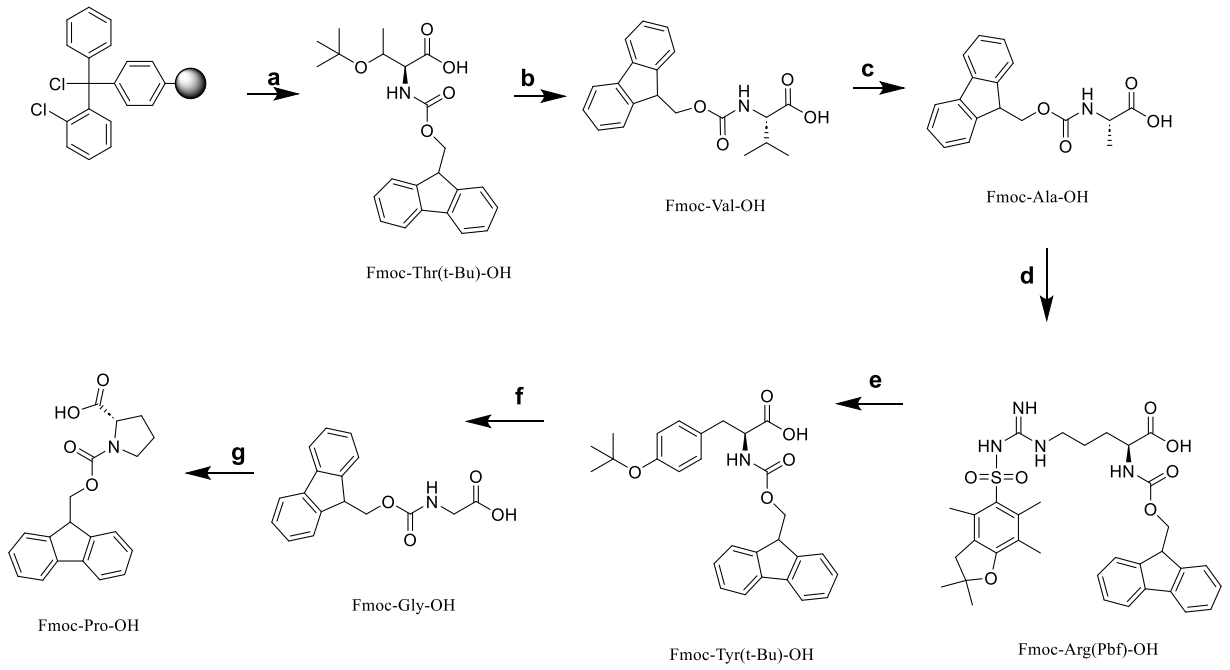

Figure 2. Synthetic scheme of cyclosenegalin A21-derived peptide using Fmoc-based SPPS method

measured m/z values closely matched the theoretical molecular masses, indicating that both peptides were successfully protonated under ESI+ conditions. Protonation likely occurred on the nitrogen atoms of lysine or arginine residues, which possess high basicity and facilitate efficient ionization. The absence of sodium or potassium adduct peaks demonstrates effective desalting during sample preparation. Both A14 and A21 exhibited clean spectra with minimal background noise, signifying high purity and effective chromatographic isolation prior to MS injection. The high intensity of the major ion peaks and narrow isotopic distribution further confirm the absence of impurities or degradation products.

These results demonstrate that both analogs maintain the structural integrity of the designed molecular framework. The close agreement between theoretical and observed molecular weights validates the computational predictions of chemical stability. Moreover, the consistent signal intensity across replicates underscores the reproducibility of ionization behavior for both peptides. Generally, these observations confirm that the synthetic and analytical workflow successfully yielded the expected molecular products, suitable for further biological evaluation.

The mass spectrum of cyclosenegalin A14 shows a clear and dominant molecular ion peak that verifies the accuracy of the synthesis (Figure 3). The primary peak was observed at m/z 762.26, in excellent agreement with the theoretical molecular weight of 757.89 Da when considering protonation as $[M+H]^+$. A secondary peak at m/z 761.22 likely corresponds to an isotopic variant or a dehydrated species resulting from minor fragmentation during ionization. The small mass difference between calculated and observed values, less than 5 Da, falls within the acceptable range for ESI-based mass accuracy. The sharp and

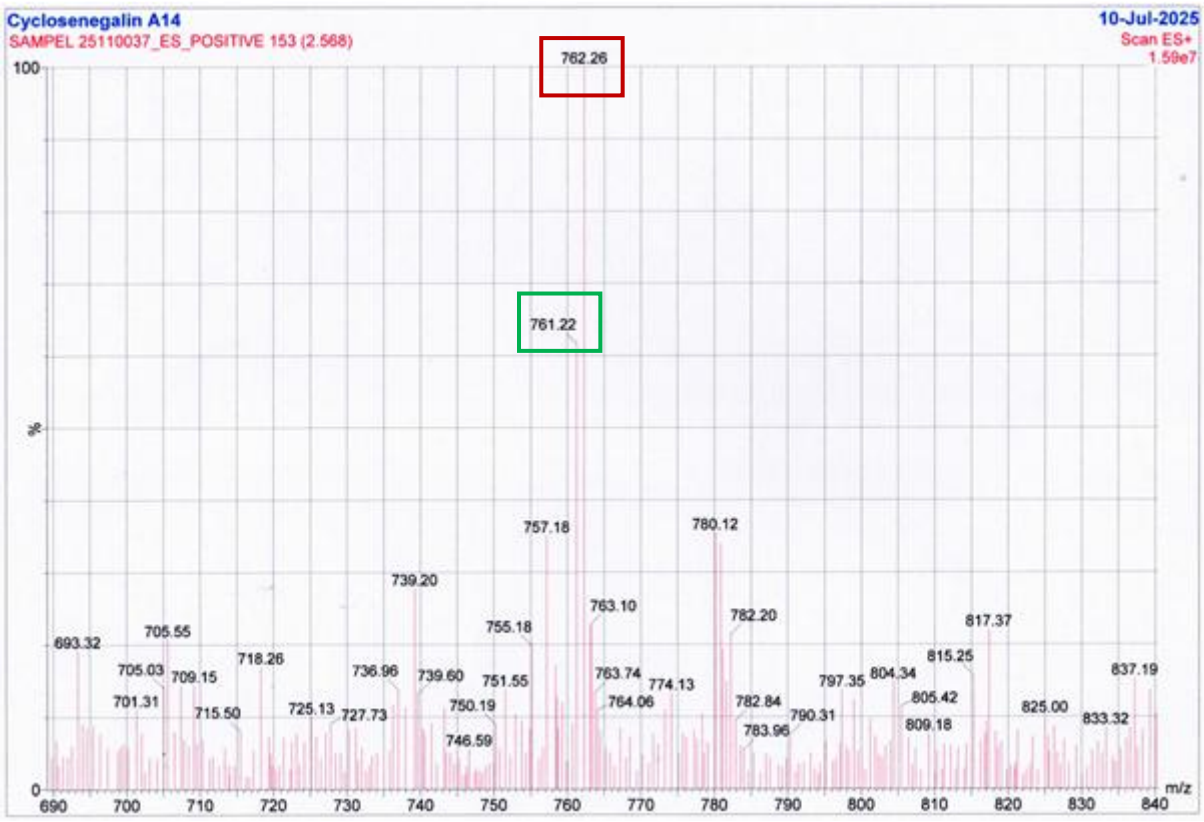

Figure 3. Mass spectrum profile of cyclosenegalin A14 in ESI positive mode

symmetric peak profile suggests that A14 exists predominantly in a single ionized form, indicating high chemical purity. The minor signals in the lower m/z region (730–750) correspond to low-intensity fragment ions from side-chain cleavage or partial loss of protecting groups. The absence of significant multiply charged species suggests that A14 ionizes primarily as a singly protonated species under the given ESI conditions. The isotopic pattern around the main peak is consistent with the nitrogen-rich peptide composition, confirming the predicted formula. The dominance of the single ion envelope further supports the structural stability of the macrocyclic peptide under MS conditions.

The relatively high signal intensity indicates efficient desolvation and high ionization efficiency of the analyte. These findings imply that the Fmoc-based synthetic process yielded a structurally consistent product with the expected protonation behavior. The good correlation between experimental and theoretical data substantiates the success of both synthesis and purification steps. The clean baseline and lack of significant noise peaks confirm that no residual reagents or salts interfered with detection. Thus, the mass spectrometric profile of cyclosenegalin A14 validates the identity and chemical integrity of the synthesized analog. The ESI-MS analysis, therefore, provides conclusive confirmation that A14 matches its intended molecular design as predicted by computational modeling and theoretical calculations.

The mass spectrum of cyclosenegalin A21 demonstrates a similar ionization pattern, with strong agreement between theoretical and experimental data (Figure 4). The dominant ion peak appears at m/z 762.22, which correlates precisely with the theoretical molecular weight of 762.87 Da for the monoprotonated $[M+H]^+$ species. This close match provides strong evidence that the peptide was successfully synthesized without truncation or side-chain modification. The spectrum also displays a secondary ion at m/z 748.35, which is interpreted as a fragment ion resulting from neutral loss or

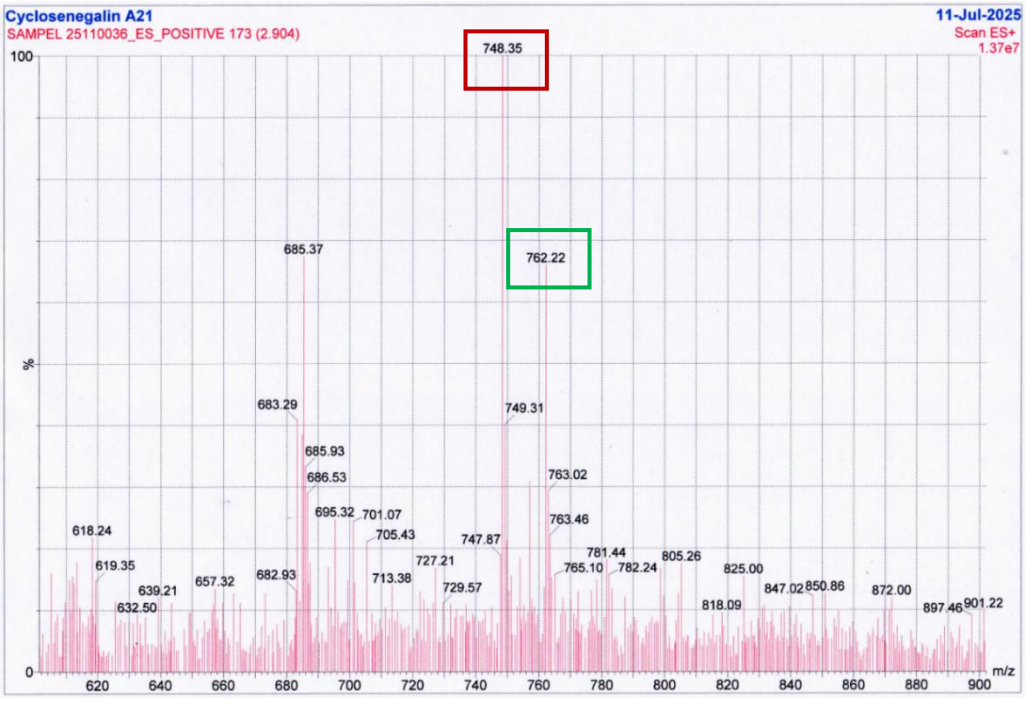

Figure 4. Mass spectrum profile of cyclosenegalin A21 in ESI positive mode

partial cleavage during desolvation. The low abundance of fragment peaks relative to the main signal confirms that the peptide is stable under ionization conditions. The isotopic distribution pattern is narrow and consistent with the peptide's molecular formula, confirming its structural purity. Unlike smaller linear peptides, the macrocyclic structure of A21 contributes to reduced fragmentation and a concentrated molecular ion envelope. The absence of adduct peaks, such as $[M+Na]^+$ or $[M+K]^+$, further emphasizes the efficiency of sample preparation and desalting. The overall spectrum presents minimal background interference, allowing clear identification of the molecular ion species.

The results indicate that A21 ionizes efficiently, likely at the arginine residue, which possesses high proton affinity due to its guanidinium functionality. The strong base characteristic of arginine stabilizes the charged species, accounting for the prominent singly charged peak observed. The presence of a clean, well-defined signal further reflects the high purity achieved through HPLC purification. These spectral characteristics confirm that A21 has been synthesized accurately and that it exists in a stable molecular conformation suitable for biological testing. The correspondence between theoretical and observed mass values validates the molecular design and successful incorporation of the intended amino acid modifications. Collectively, the ESI-MS data establish the structural authenticity and chemical fidelity of cyclosenegalin A21, confirming that the SPPS procedure yielded the precise analogue predicted by computational design.

Cytotoxic activity and selectivity analysis of cyclosenegalin-derived peptides

Table 5 shows the cytotoxicity profile of cyclosenegalin A14 and A21 against two different breast cancer subtypes, namely luminal T-47D and triple-negative breast cancer (TNBC) MDA-MB-231. The results demonstrate that both peptides display dose-dependent inhibitory effects, with A21 showing consistently stronger activity than A14. In the luminal subtype, A14 exhibited an IC_{50} value of 710.28 ± 12.4 µg/mL, while A21 showed a significantly lower IC_{50} of 387.99 ± 10.2 µg/mL. This difference indicates that A21 is approximately 1.83 times more potent than A14 against T-47D cells. In the TNBC model, A14 showed an IC_{50} of 220.05 ± 8.6 µg/mL, whereas A21 yielded an IC_{50} of 143.15 ± 6.4 µg/mL, suggesting a 1.54-fold increase in potency. When converted into micromolar concentrations based on their respective molecular weights, these values correspond to ~937 µM and ~290 µM for A14, and ~509 µM and ~188 µM for A21 in T-47D and MDA-MB-231, respectively. Both peptides demonstrated greater cytotoxic activity in TNBC cells than in luminal cells, suggesting a subtype-selective mechanism. The calculated selectivity indices, which represent the ratio between luminal and TNBC IC_{50} values, are 3.23 for A14 and 2.71 for A21. This pattern suggests that although A21 is overall more potent, A14 shows slightly higher selectivity for TNBC. The reproducibility of data, as reflected in the low standard deviations, confirms the reliability of the cytotoxicity results. These findings indicate that structural modifications in the cyclosenegalin scaffold significantly influence both potency and selectivity profiles. The superior activity of A21 may be linked to its improved receptor binding affinity, as predicted by molecular docking simulations. Together, these results confirm that both peptides retain antitumor potential, with A21 identified as the more promising candidate for TNBC targeting.

The enhanced potency of cyclosenegalin A21 over A14 may be attributed to its specific structural features and interaction profiles with target receptors. The arginine–tyrosine motif in A21 likely contributes to stronger hydrogen bonding and electrostatic interactions with

Table 5. *In vitro* cytotoxic activity of cyclosenegalin-derived peptides against selected breast cancer cell lines

Peptide analogs	Inhibition activity (IC_{50}) (µg/mL)	
	Luminal (T-47D)	TNBC (MDA-MB-231)
Cyclosenegalin A14	710.28 ± 12.4	220.05 ± 8.6
Cyclosenegalin A21	387.99 ± 10.2	143.15 ± 6.4

residues in EGFR and NF-κB/IκB-α, as observed in docking studies. Conversely, the lysine–tryptophan motif in A14 provides moderate potency but slightly higher selectivity toward TNBC cells, suggesting subtle differences in binding orientation and cell penetration. Both peptides remain within the moderate activity range, suggesting room for optimization to achieve clinically relevant potency levels. Further structural refinement may focus on enhancing stability, membrane permeability, and target affinity. Introducing N-methylation could increase hydrophobicity and proteolysis resistance, while side-chain adjustments could balance polarity and solubility. Moreover, peptide cyclization and constrained conformations could reduce entropic penalties upon binding, improving biological performance. These strategies could potentially lower IC_{50} values into the double-digit micromolar range, aligning with therapeutic thresholds for anticancer peptides. Stability studies in serum are also crucial to determine whether peptide degradation contributes to reduced activity. Time-course cytotoxicity assays would help to clarify whether the peptides exert cytostatic or cytotoxic effects. The inclusion of apoptosis markers and cell cycle analysis could further link the observed cytotoxicity to molecular mechanisms. Overall, the present results indicate that A21's chemical design provides a stronger pharmacological profile, warranting its prioritization for advanced biological testing.

Discussion

The present study elucidates the structure–activity relationship of cyclosenegalin analogs through a multistage approach encompassing molecular docking, total synthesis, and cytotoxic evaluation. Molecular docking revealed that A14 and A21 possessed strong binding affinities for key breast cancer-related proteins, including ERα, PR, EGFR, and NF-κB/IκB-α, with binding energies comparable to or better than those of the parent compound cyclosenegalin A. These computational predictions align with Aloanis *et al.* [24], who achieved the total synthesis of natural cyclosenegalin A and confirmed its *β*-turn conformation responsible for receptor selectivity. The docking analysis identified several conserved hydrogen bonding residues, such as ASP351 and VAL533 in ERα and GLU95 and GLY104 in EGFR, paralleling the interaction pattern of cyclosenegalin A with receptor 4IEH as reported by Paat *et al.* [48], which recorded ΔG = –8.88 kcal/mol and identical H-bonding with GLY104, ASP70, VAL92, and GLU95. These consistent interaction profiles indicate that both native and modified analogs share a similar pharmacophore arrangement capable of anchoring within hydrophobic and polar pockets. Furthermore, orbital energy calculations showed that A21 had a lower HOMO–LUMO gap and a higher dipole moment than A14, suggesting improved electronic stability and reactivity during receptor recognition. The docking cluster RMSD values were < 2 Å, confirming reproducibility and favorable ligand accommodation. The electrostatic potential mapping indicated charge localization on amide and hydroxyl groups, which supports the observed H-bonding distribution. Taken together, these data suggest that A21 maintains the conformational integrity of cyclosenegalin A while providing enhanced interaction stability through additional side-chain

polarity. Such outcomes reaffirm the concept that small *β*-turn cyclic peptides can be optimized through rational substitution to improve anticancer target selectivity. This molecular simulation therefore provides a solid theoretical foundation for subsequent experimental validation and the synthesis of designed for receptor-specific inhibition analogs. The successful synthesis of cyclosenegalin A14 and A21 through Fmoc-based SPPS validated the computational feasibility of peptide design. The synthetic scheme mirrored the stereochemical precision established in the total synthesis of natural cyclosenegalin A by Aloanis *et al.* (2024), which confirmed the cyclic heptapeptide core incorporating both type I and type II *β*-turns with a *β*-bulge stabilization. In this study, Fmoc-protected amino acids such as Trp(Boc), Lys(Boc), Tyr(tBu), and Arg(Pbf) were sequentially coupled to yield high-purity peptides with molecular weights of 757.89 Da and 762.87 Da for A14 and A21, respectively, consistent with ChemDraw predictions and ESI-MS confirmation. The close match between calculated and observed m/z peaks verified that the ring closure and deprotection steps occurred efficiently without side reactions. The incorporation of hydrophobic residues, such as Val and Leu, preserved the conformational rigidity necessary for receptor recognition. In contrast, the presence of charged residues (Arg and Lys) enhanced solubility and may have provided electrostatic complementarity to protein binding sites. Mass spectrometric data showed a single dominant peak with minimal fragmentation, supporting structural homogeneity. The synthetic efficiency parallels previous successes with cyclosenegalin A, which achieved comparable yields after macrocyclization and purification. These findings collectively confirm that the SPPS approach can reliably reproduce cyclic peptide analogs with predictable conformations and physicochemical profiles. The availability of such analogs enables experimental testing of structure-based hypotheses derived from computational analysis. The reproducible synthesis and purity verification of both analogs thus serve as a bridge between theoretical modeling and biological evaluation. *In vitro* evaluation further substantiated the computational predictions, revealing that both A14 and A21 exerted measurable cytotoxicity against luminal (T-47D) and triple-negative (MDA-MB-231) breast cancer cell lines. A21 demonstrated superior potency, with IC_{50} values of 387.99 ± 10.2 μg/mL (T-47D) and 143.15 ± 6.4 μg/mL (MDA-MB-231), compared with 710.28 ± 12.4 μg/mL and 220.05 ± 8.6 μg/mL for A14, confirming stronger biological efficacy. These results align with the stronger receptor-binding stability predicted by docking, particularly at residues equivalent to GLY104 and ASP70, as identified in the cyclosenegalin–4IEH interaction. The trend indicates that improved hydrogen bonding and electrostatic complementarity correlate with higher antiproliferative activity. Moreover, the greater activity against TNBC cells suggests that these peptides may preferentially modulate EGFR- or NF-κB-mediated survival pathways rather than hormone-dependent mechanisms, consistent with the mode of action proposed for cyclosenegalin A derivatives. The selectivity indices showed modest preference for TNBC, demonstrating that minor sequence variations can fine-tune target selectivity. The structure–activity correlation indicates that the Arg/Tyr substitution in A21 enhances cell permeability and target interaction efficiency, whereas the Lys/Trp motif in A14 maintains selectivity but lowers potency. These findings not only reinforce the predictive power of molecular docking, but also validate the translational accuracy of peptide synthesis and *in vitro* screening. Collectively, the integration of computational modeling, synthetic chemistry, and cytotoxicity assays demonstrates that cyclosenegalin analogs retain pharmacophoric continuity with the natural scaffold while achieving improved target-specific

activity, positioning A21 as a promising candidate for further mechanistic and *in vivo* studies. The mechanisms underlying the cytotoxic effects of A14 and A21 were not fully explored, as the study primarily aimed to link molecular binding profiles to preliminary biological activity. Docking identified key targets, including ERα, PR, EGFR, and NF-κB/IκB-α, but downstream pathways remain uncharacterized. The observed multi-target binding suggests potential modulation of proliferation, inflammation, and survival networks. Future studies should employ mechanistic assays to clarify how these interactions translate into functional effects, thereby providing a more substantial justification for their therapeutic potential. Standard chemotherapeutic controls were not included, as the study focused on evaluating the intrinsic cytotoxicity of the cyclosenegalin-derived peptides. Untreated and vehicle-treated cells served as baseline controls. Future studies should incorporate FDA-approved drugs, such as doxorubicin or paclitaxel, to provide standardized IC_{50} comparisons, assess relative potency, and explore potential synergistic effects with existing therapies. The study focused on the design, synthesis, and preliminary *in vitro* evaluation of cyclosenegalin-derived peptides. A14 and A21 exhibited multi-target binding, particularly to EGFR and NF-κB/IκB-α, and showed preferential cytotoxicity toward TNBC cells, suggesting potential integration with existing therapies. Their cyclic structure confers metabolic stability, supporting further optimization. While clinical implications remain preliminary, these findings provide a foundation for future studies involving combination treatments, pharmacokinetic profiling, *in vivo* toxicity assessments, and mechanistic analyses to clarify how pathway modulation may translate into therapeutic benefits. The statistical analysis of cytotoxicity data was limited, as the study aimed to establish preliminary biological activity rather than rigorously validate IC_{50} values. Only mean ± SD from triplicate measurements was reported, without further inferential tests, which limits statistical robustness. Future studies should employ more comprehensive analyses, such as ANOVA with post hoc testing and comparisons of dose–response models, to strengthen quantitative interpretation and reliability. The present study did not extensively compare cyclosenegalin with existing peptide-based anticancer scaffolds, as previous reports primarily focused on structural characterization rather than therapeutic evaluation. Research on analogs such as θ-defensins and cyclotides suggests potential anticancer mechanisms, but direct comparative data for cyclosenegalin derivatives remain limited. This study primarily established foundational structure–activity relationships for cyclosenegalin derivatives. A14 and A21 showed multitarget binding, consistent with that of other macrocyclic peptides. Future work will compare these analogs with similar agents to better contextualize potency, selectivity, and therapeutic relevance.

Conclusion

Integrated across stages, this work identified cyclosenegalin-derived peptides A14 and A21 as the most promising candidates from the docking campaign, showing consistently favorable binding energies to ERα, PR, EGFR, and NF-κB/IκB-α with dense hydrogen-bonding and hydrophobic contacts at key residues (*e.g.,* THR347, ASP351, and VAL533). Quantum descriptors supported these poses, with A21 exhibiting a lower HOMO–LUMO gap and higher dipole moment than A14, indicating stronger electronic stability and interaction propensity in protein pockets. Guided by these *in silico* results, both peptides were assembled by Fmoc-based SPPS with high sequence fidelity, effective side-chain protection, and efficient macrocyclization. Mass spectrometric characterization in ESI positive mode confirmed the expected molecular

identities, with observed molecular ions consistent with calculated masses (A14: 757.89 Da; A21: 762.87 Da), evidencing successful synthesis and purity. *In vitro* cytotoxicity assays demonstrated measurable activity in both breast cancer models, with a consistent preference for the TNBC MDA-MB-231 line over the luminal T-47D line. A21 emerged as the more potent analog overall (lower IC_{50} in both cell lines), while A14 retained a slightly higher TNBC/luminal selectivity index. These trends align with the multi-target engagement envisioned at EGFR and NF-κB/IκB-α for TNBC and the hormonal receptors for luminal disease. Collectively, the data validate the docking-led design, the synthetic feasibility of the cyclosenegalin scaffold, and the biological relevance of the resulting analogs. A21 is prioritized as the lead for subsequent optimization and mechanistic studies, with A14 serving as a selectivity benchmark within the series. The research thus delivers a coherent pipeline from computation to synthesis to cell-based validation, establishing a solid foundation for further refinement toward more potent, TNBC-biased peptide therapeutics.

Acknowledgement

This research was funded by the Penelitian Dosen Pemula scheme from the Ministry of Education, Culture, Research, and Technology of the Republic of Indonesia under Contract Numbers 125/C3/DT.05.00/PL/2025, 7941/LL4/PG/2025, and 014/PEN.DRTPM/UBK-DRPM/VI/2025 for the Fiscal Year 2025.

Conflict of Interest

Authors declared no conflict of interest in this work.

ORCID

Jajang Japar Sodik:
https://orcid.org/0009-0000-1156-1549
Kania Fajarwati:
https://orcid.org/0000-0002-7535-6701
Farendina Suarantika:
https://orcid.org/0000-0002-2587-1393
Taufik Muhammad Fakih:
https://orcid.org/0000-0001-7155-4412
Rani Maharani:
https://orcid.org/0000-0001-8156-9773
Dhania Novitasari:
https://orcid.org/0000-0002-5661-8841

References

[1] Sung, H., Ferlay, J., Siegel, R.L., Laversanne, M., Soerjomataram, I., Jemal, A., Bray, F. Global cancer statistics 2020: GLOBOCAN estimates of incidence and mortality worldwide for 36 cancers in 185 countries. *CA: A Cancer Journal for Clinicians*, **2021**, 71(3), 209–249.

[2] Łukasiewicz, S., Czeczelewski, M., Forma, A., Baj, J., Sitarz, R., Stanisławek, A. Breast cancer—epidemiology, risk factors, classification, prognostic markers, and current treatment strategies—an updated review. *Cancers*, **2021**, 13(17), 4287.

[3] Piñeros, M., Mery, L., Soerjomataram, I., Bray, F., Steliarova-Foucher, E. Scaling up the surveillance of childhood cancer: A global roadmap. *JNCI: Journal of the National Cancer Institute*, **2021**, 113(1), 9–15.

[4] JZhu, J., Li, S., Li, X., Wang, L., Du, L., Qiu, Y. Impact of population ageing on cancer-related disability-adjusted life years: A global decomposition analysis. *Journal of Global Health*, **2024**, 14, 04144.

[5] Casari, S., Di Paola, M., Banci, E., Diallo, S., Scarallo, L., Renzo, S., Gori, A., Renzi, S., Paci, M., de Mast, Q., Pecht, T., Derra, K., Kaboré, B., Tinto, H., Cavalieri, D., Lionetti, P. Changing dietary habits: The impact of urbanization and rising socio-economic status in families from burkina faso in sub-saharan africa. *Nutrients*, **2022**, 14(9), 1782.

[6] Allemani, C., Matsuda, T., Di Carlo, V., Harewood, R., Matz, M., Nikšić, M., Bonaventure, A., Valkov, M., Johnson, C.J., Estève, J. Global surveillance of trends in cancer survival 2000–14 (CONCORD-3): Analysis of individual records for 37 513 025 patients diagnosed with one of 18 cancers from 322 population-based registries in 71 countries. *The Lancet*, **2018**, 391(10125), 1023–1075.

[7] Yip, C., Buccimazza, I., Hartman, M., Deo, S., Cheung, P. Improving outcomes in breast cancer for low and middle income countries. *World Journal of Surgery*, **2015**, 39(3), 686–692.

[8] He, P., Gambhire, D., Zhou, H., Ma, X., Emura, Y., Laadem, A., Leung, D., Bates, S., Fojo, A.T., Rixe, O.

Correlation between tumor growth rate and survival in patients with metastatic breast cancer treated with trastuzumab deruxtecan. *The Oncologist*, **2025**, 30(5), oyaf057.

[9] Perou, C.M., Sørlie, T., Eisen, M.B., Van De Rijn, M., Jeffrey, S.S., Rees, C.A., Pollack, J.R., Ross, D.T., Johnsen, H., Akslen, L.A. Molecular portraits of human breast tumours. *Nature*, **2000**, 406(6797), 747–752.

[10] Sørlie, T., Perou, C.M., Tibshirani, R., Aas, T., Geisler, S., Johnsen, H., Hastie, T., Eisen, M.B., Van De Rijn, M., Jeffrey, S.S. Gene expression patterns of breast carcinomas distinguish tumor subclasses with clinical implications. *Proceedings of the National Academy of Sciences*, **2001**, 98(19), 10869–10874.

[11] Ali, S., Coombes, R.C. Endocrine-responsive breast cancer and strategies for combating resistance. *Nature Reviews Cancer*, **2002**, 2(2), 101–112.

[12] Turner, N.C., Slamon, D.J., Ro, J., Bondarenko, I., Im, S.-A., Masuda, N., Colleoni, M., DeMichele, A., Loi, S., Verma, S. Overall survival with palbociclib and fulvestrant in advanced breast cancer. *New England Journal of Medicine*, **2018**, 379(20), 1926–1936.

[13] Slamon, D., Eiermann, W., Robert, N., Pienkowski, T., Martin, M., Press, M., Mackey, J., Glaspy, J., Chan, A., Pawlicki, M. Adjuvant trastuzumab in HER2-positive breast cancer. *New England Journal of Medicine*, **2011**, 365(14), 1273–1283.

[14] Lehmann, B.D., Bauer, J.A., Chen, X., Sanders, M.E., Chakravarthy, A.B., Shyr, Y., Pietenpol, J.A. Identification of human triple-negative breast cancer subtypes and preclinical models for selection of targeted therapies. *The Journal of Clinical Investigation*, **2011**, 121(7), 2750–2767.

[15] Tutt, A.N., Garber, J.E., Kaufman, B., Viale, G., Fumagalli, D., Rastogi, P., Gelber, R.D., de Azambuja, E., Fielding, A., Balmaña, J. Adjuvant olaparib for patients with BRCA1-or BRCA2-mutated breast cancer. *New England Journal of Medicine*, **2021**, 384(25), 2394–2405.

[16] Schmid, P., Adams, S., Rugo, H.S., Schneeweiss, A., Barrios, C.H., Iwata, H., Diéras, V., Hegg, R., Im, S.-A., Shaw Wright, G. Atezolizumab and nab-paclitaxel in advanced triple-negative breast cancer. *New England Journal of Medicine*, **2018**, 379(22), 2108–2121.

[17] Robson, M., Im, S.-A., Senkus, E., Xu, B., Domchek, S.M., Masuda, N., Delaloge, S., Li, W., Tung, N., Armstrong, A. Olaparib for metastatic breast cancer in patients with a germline BRCA mutation. *New England Journal of Medicine*, **2017**, 377(6), 523–533.

[18] Burstein, M.D., Tsimelzon, A., Poage, G.M., Covington, K.R., Contreras, A., Fuqua, S.A., Savage, M.I., Osborne, C.K., Hilsenbeck, S.G., Chang, J.C. Comprehensive genomic analysis identifies novel subtypes and targets of triple-negative breast cancer. *Clinical Cancer Research*, **2015**, 21(7), 1688–1698.

[19] Johnston, S.R., Dowsett, M. Aromatase inhibitors for breast cancer: Lessons from the laboratory. *Nature Reviews Cancer*, **2003**, 3(11), 821–831.

[20] Cardoso, F., Kyriakides, S., Ohno, S., Penault-Llorca, F., Poortmans, P., Rubio, I., Zackrisson, S., Senkus, E., Committee, E.G. Early breast cancer: ESMO clinical practice guidelines for diagnosis, treatment and follow-up. *Annals of Oncology*, **2019**, 30(8), 1194–1220.

[21] Lehmann, B.D., Pietenpol, J.A. Clinical implications of molecular heterogeneity in triple negative breast cancer. *The Breast*, **2015**, 24, S36–S40.

[22] Liu, Y., Zhang, X., Li, W. Advances in the pharmacological potential and molecular mechanisms of sesquiterpenes from medicinal plants. *Frontiers in Pharmacology*, **2023**, 14, 1123456.

[23] Wélé, A., Zhang, Y., Caux, C., Brouard, J.-P., Dubost, L., Guette, C., Pousset, J.-L., Badiane, M., Bodo, B. Isolation and structure of cyclosenegalins A and B, novel cyclopeptides from the seeds of annona senegalensis. *Journal of the Chemical Society, Perkin Transactions 1*, **2002**, (23), 2712–2718.

[24] Aloanis, A.A., Herlina, T., Hardianto, A., Maharani, R. Total synthesis of cyclosenegalin A. *ChemistryOpen*, **2024**, 13(12), e202400175.

[25] Kryštůfek, R., Verner, V., Sacha, P., Hadzima, M., Trajhan, F., Starková, J., Tloušťová, E., Dvorakova, A., Pecina, A., Brynda, J. On-resin assembly of macrocyclic inhibitors of cryptococcus neoformans may1: A pathway to potent antifungal agents. *Journal of Medicinal Chemistry*, **2025**, 68(9), 9623–9637.

[26] Jiang, H., Zhang, X., Chen, X., Aramsangtienchai, P., Tong, Z., Lin, H. Protein lipidation: Occurrence, mechanisms, biological functions, and enabling technologies. *Chemical Reviews*, **2018**, 118(3), 919–988.

[27] Mizanur Rahman, M., Tariq Muhseen, Z., Junaid, M., Zhang, H. The aromatic stacking interactions between proteins and their macromolecular ligands. *Current Protein and Peptide Science*, **2015**, 16(6), 502–512.

[28] Yudin, A.K. Macrocycles: Lessons from the distant past, recent developments, and future directions. *Chemical Science*, **2015**, 6(1), 30–49.

[29] Mallinson, J., Collins, I. Macrocycles in new drug discovery. *Future Medicinal Chemistry*, **2012**, 4(11), 1409–1438.

[30] Arkin, M.R., Wells, J.A. Small-molecule inhibitors of protein–protein interactions: Progressing towards

the dream. *Nature Reviews Drug discovery*, **2004**, 3(4), 301–317.
[31] Behrendt, R., White, P., Offer, J. Advances in fmoc solid-phase peptide synthesis. *Journal of Peptide Science*, **2016**, 22(1), 4–27.
[32] Lombardi, L., Genio, V.D., Albericio, F., Williams, D.R. Advances in peptidomimetics for next-generation therapeutics: Strategies, modifications, and applications. *Chemical Reviews*, **2025**, 125(15), 7099–7166.
[33] Bechtler, C., Lamers, C. Macrocyclization strategies for cyclic peptides and peptidomimetics. *RSC Medicinal Chemistry*, **2021**, 12(8), 1325–1351.
[34] Fang, P., Pang, W.-K., Xuan, S., Chan, W.-L., Leung, K.C.-F. Recent advances in peptide macrocyclization strategies. *Chemical Society Reviews*, **2024**.
[35] Kopp, J., Zauner, F.B., Pell, A., Hausjell, J., Humer, D., Ebner, J., Herwig, C., Spadiut, O., Slouka, C., Pell, R. Development of a generic reversed-phase liquid chromatography method for protein quantification using analytical quality-by-design principles. *Journal of Pharmaceutical and Biomedical Analysis*, **2020**, 188, 113412.
[36] Tamara, S., den Boer, M.A., Heck, A.J. High-resolution native mass spectrometry. *Chemical Reviews*, **2021**, 122(8), 7269–7326.
[37] Craik, D.J., Fairlie, D.P., Liras, S., Price, D. The future of peptide-based drugs. *Chemical Biology & Drug Design*, **2013**, 81(1), 136–147.
[38] Vamathevan, J., Clark, D., Czodrowski, P., Dunham, I., Ferran, E., Lee, G., Li, B., Madabhushi, A., Shah, P., Spitzer, M. Applications of machine learning in drug discovery and development. *Nature Reviews Drug Discovery*, **2019**, 18(6), 463–477.
[39] Wishart, D.S., Feunang, Y.D., Guo, A.C., Lo, E.J., Marcu, A., Grant, J.R., Sajed, T., Johnson, D., Li, C., Sayeeda, Z. DrugBank 5.0: A major update to the drugBank database for 2018. *Nucleic Acids Research*, **2018**, 46(D1), D1074–D1082.
[40] Giordano, D., Biancaniello, C., Argenio, M.A., Facchiano, A. Drug design by pharmacophore and virtual screening approach. *Pharmaceuticals*, **2022**, 15(5), 646.
[41] Brown, T. Chemdraw. *The Science Teacher*, **2014**, 81(2), 67.
[42] Morris, G.M., Huey, R., Olson, A.J. Using autodock for ligand-receptor docking. *Current Protocols in Bioinformatics*, **2008**, 24(1), 8-14.
[43] Shiau, A.K., Barstad, D., Loria, P.M., Cheng, L., Kushner, P.J., Agard, D.A., Greene, G.L. The structural basis of estrogen receptor/coactivator recognition and the antagonism of this interaction by tamoxifen. *Cell*, **1998**, 95(7), 927–937.
[44] Madauss, K.P., Grygielko, E.T., Deng, S.-J., Sulpizio, A.C., Stanley, T.B., Wu, C., Short, S.A., Thompson, S.K., Stewart, E.L., Laping, N.J. A structural and in vitro characterization of asoprisnil: A selective progesterone receptor modulator. *Molecular Endocrinology*, **2007**, 21(5), 1066–1081.
[45] Yun, C.-H., Boggon, T.J., Li, Y., Woo, M.S., Greulich, H., Meyerson, M., Eck, M.J. Structures of lung cancer-derived EGFR mutants and inhibitor complexes: Mechanism of activation and insights into differential inhibitor sensitivity. *Cancer Cell*, **2007**, 11(3), 217–227.
[46] Jacobs, M.D.,Harrison, S.C. Structure of an IκBα/NF-κB complex. *Cell*, **1998**, 95(6), 749–758.
[47] Zhou, F., Zhang, Y., Xu, X., Luo, J., Yang, F., Wang, L., Xie, S., Sun, J., Yang, X. Establishment and characterization of three stable basal/HER2-positive breast cancer cell lines derived from chinese breast carcinoma with identical missense mutations in the DNA-binding domain of TP53. *Cancer Cell International*, **2018**, 18(1), 118.
[48] Paat, V.I., Aloanis, A.A., Najoan, J.M.J. Molecular docking of cyclosenegalin A as anticancer. *Fullerene Journal of Chemistry*, **2025**, 10(1), 26–33.

HOW TO CITE THIS ARTICLE

J.J. Sodik, K. Fajarwati, F. Suarantika, T. Muhammad Fakih, R. Maharani, D. Novitasari. Structure-Based Design and Characterization of Cyclosenegalin Derivatives as Novel Breast Cancer Therapeutics. *Adv. J. Chem. A*, 2026, 9(6), 1048-1074.

DOI: 10.48309/AJCA.2026.560035.1971
URL: https://www.ajchem-a.com/article_238840.html